Article | Open Access

Energy Materials

Huang *et al. Energy Mater.* **2026**, *6*, 600110 **DOI:**10.20517/energymater.2026.227

Robust double-lock MXene anodes for stable sodium storage

Xuan Huang[1,2], Jiaqi Fei[1], Lingxia Fan[2], Lize Zhang[2], Xinghui Sun[2], Junfan Zhang[2], Chunguang Wei[2], Hongwei Bi[2,*], Aruuhan Bayaguud[1,*], Yelong Zhang[2,*]

Keywords:
MXene, terephthalaldehyde, double-lock effect, sodium-ion batteries, electrochemical performance

Citation: Huang, X.; Fei, J.; Fan, L.; Zhang, L.; Sun, X.; Zhang, J.; Wei, C.; Bi, H.; Bayaguud, A.; Zhang, Y. Robust double-lock MXene anodes for stable sodium storage. *Energy Mater.* **2026**, *6*, 600110. https://dx.doi.org/10.20517/energymater.2026.227

Received: 17 Jul 2026
Accepted: 14 Aug 2026
Published: 27 Aug 2026

Academic Editor:
Yuping Wu
Copy Editor:
Fangling Lan
Production Editor:
Fangling Lan

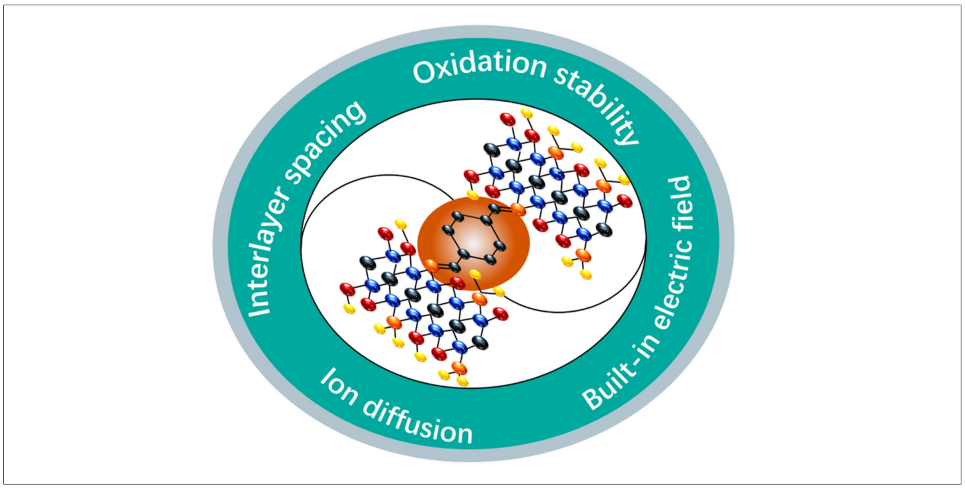

Abstract

Although MXenes possess intrinsically high electrical conductivity and a layered architecture favorable for charge storage, their practical use is still hindered by severe nanosheet restacking, susceptibility to oxidation, limited electrochemically active sites, and slow ion-diffusion kinetics. Herein, a facile molecular grafting strategy is used to covalently anchor terephthalaldehyde (TPAL) within aminated Ti_3C_2 MXene interlayers, constructing a Ti_3C_2-TPAL composite with a well-defined double-lock effect. The first lock arises from imine-bond-based covalent anchoring between TPAL and aminated Ti_3C_2, which suppresses sheet restacking and interlayer slippage. The second lock arises from the rigid aromatic TPAL pillars, which enlarge the interlayer galleries and help maintain the spacing during repeated Na^+ storage. This regulated architecture enables Ti_3C_2-TPAL to provide 57.0 mAh g^{-1} at 10 A g^{-1}. During extended cycling at 5 A g^{-1}, the electrode still outputs 54.3 mAh g^{-1} over 2,500 cycles, indicating enhanced rate tolerance and long-cycle stability. TPAL effectively suppresses the breathing effect of MXene. In addition, interfacial charge redistribution caused by TPAL grafting may enhance the interaction with Na^+ and promote more favorable charge-transfer kinetics. Moreover, the assembled Ti_3C_2-

[1]School of Materials Science and Engineering, Inner Mongolia University of Technology, Hohhot 010051, Inner Mongolia, China.
[2]School of New Energy, Inner Mongolia University of Technology, Ordos 017010, Inner Mongolia, China.

***Correspondence to:** Dr. Hongwei Bi, Prof. Yelong Zhang, School of New Energy, Inner Mongolia University of Technology, Ordos 017010, Inner Mongolia, China. E-mail: bhw@imut.edu.cn; ylzhang@imut.edu.cn; Prof. Aruuhan Bayaguud, School of Materials Science and Engineering, Inner Mongolia University of Technology, Hohhot 010051, Inner Mongolia, China. E-mail: jinaruhan@imut.edu.cn

TPAL||$Na_4Fe_3(PO_4)_2(P_2O_7)$ full cell exhibits an energy density of 190.8 Wh kg^{-1} and a power density of 9,040 W kg^{-1} based on the mass of the cathode active material. The present study illustrates that molecular grafting can be used to regulate MXene interlayers and enhance their applicability as sodium-ion battery anodes.

INTRODUCTION

As clean energy systems continue to expand, large-scale energy storage has become essential for smoothing the intermittent and fluctuating output of solar and wind power. In this context, sodium-ion batteries (SIBs) offer a practical route for stationary storage owing to the low cost, wide availability, and lithium-like electrochemical characteristics of sodium[1,2]. Consequently, SIBs demonstrate broad application prospects in smart grids, consumer electronics, and electric transportation. The electrochemical behavior of the anode directly affects the usable capacity, long-term stability, and high-rate response of SIBs. Its performance acts as a bottleneck restricting the industrialization process of SIBs. Anodes explored for SIBs can be broadly classified into carbonaceous materials[3,4], alloying-type systems[5,6], metal-based compounds[7-9], and two-dimensional (2D) layered structures[10,11]. However, the critical drawbacks of traditional carbon-based materials (low capacity), alloy-type materials (severe volume expansion), and metal compounds (poor conductivity) render them inadequate for the demands of high-performance SIB applications. Accordingly, designing advanced anodes and developing effective modification strategies have become key research directions in the SIB field[12,13].

As typical two-dimensional transition-metal carbides, nitrides, and carbonitrides, MXenes possess layered frameworks, metallic conductivity, mechanical robustness, and chemically tunable surface groups[14-17]. Since the first MXene was reported in 2011, this material family has been increasingly explored for SIB anodes[18]. Despite these advantages, MXene-based electrodes still suffer from inherent structural drawbacks that limit their practical performance. Specifically, van der Waals attraction between neighboring MXene layers promotes restacking, which reduces accessible surface area and active-site exposure while limiting fast Na^+ diffusion within the interlayer channels[19-21]. Meanwhile, the limited diversity and low reactivity of surface terminations on MXenes lead to weak electrolyte compatibility and make the layered structure prone to collapse during repeated cycling[22,23], thereby compromising prolonged electrochemical durability. To address these issues, researchers have developed various modification strategies[24,25]. Among them, grafting modification is considered one of the most promising methods due to its ability to precisely regulate surface chemical properties, effectively inhibit sheet restacking, and introduce new active sites[26-28]. Compared with other organic cross-linkers, terephthalaldehyde (TPAL) offers several structural advantages for regulating MXene interlayers. Aliphatic dialdehydes, such as glutaraldehyde, can react with amino groups but their flexible chains may not provide sufficient rigidity to stabilize the interlayer spacing. Monofunctional aromatic aldehydes can introduce aromatic units but cannot effectively bridge adjacent MXene sheets. Other aromatic dialdehydes, such as phthalaldehyde or isophthalaldehyde, may also form imine linkages, but their different aldehyde positions lead to less linear molecular geometries. In contrast, TPAL contains two para-positioned aldehyde groups and a rigid benzene backbone, enabling covalent coupling with aminated Ti_3C_2 while serving as a molecular pillar to stabilize the expanded interlayer spacing. Therefore, TPAL was selected as a representative aromatic dialdehyde cross-linker to construct the double-lock interlayer structure. In principle, TPAL grafting may provide additional active sites, reinforce Na^+ adsorption, and stabilize the electrode/electrolyte contact during cycling. Nevertheless, TPAL-grafted MXene anodes for SIBs remain insufficiently explored, and both the grafting process and the Na-storage behavior require further clarification.

In this work, TPAL is covalently grafted within aminated Ti_3C_2 MXene interlayers to construct a Ti_3C_2-TPAL composite with a well-defined double-lock architecture. The double-lock effect is defined as the combination of covalent anchoring and rigid interlayer pillaring. The imine bonds formed between TPAL and aminated

Ti_3C_2 serve as the first lock, chemically anchoring the MXene sheets and suppressing restacking or interlayer slippage. The rigid aromatic TPAL molecules serve as the second lock, acting as molecular pillars to enlarge and stabilize the Ti_3C_2 interlayer spacing. The improved oxidation resistance, interfacial charge redistribution, and enhanced Na^+ transport kinetics are therefore discussed as consequences of this double-lock structure rather than as separate components of the double-lock effect. By combining *in situ* X-ray diffraction (XRD), Distribution of relaxation times (DRT) analysis, and simplified density functional theory (DFT) calculations, the role of TPAL in stabilizing the Ti_3C_2 interlayers and improving Na-storage kinetics is investigated from both experimental and theoretical perspectives. The coordinated regulation of the interlayer structure and Na-storage kinetics gives Ti_3C_2-TPAL favorable electrochemical performance in SIB half cells, including 57.0 mAh g^{-1} at 10 A g^{-1} and 54.3 mAh g^{-1} after 2,500 cycles at 5 A g^{-1}. Pairing with a $Na_4Fe_3(PO_4)_2(P_2O_7)$ (NFPP) cathode, this configuration reaches cathode-mass-normalized energy and power densities of 190.8 Wh kg^{-1} and 9,040 W kg^{-1}, respectively. The molecular-grafting-induced double-lock architecture reported here offers a useful strategy for constructing advanced 2D-material-based anodes for SIBs.

EXPERIMENTAL

Preparation of MXene

Ti_3C_2 MXene was obtained from MAX through hydrofluoric acid (HF)-assisted selective Al extraction. Briefly, 3 g of Ti_3AlC_2 MAX was gradually dispersed in portions within 60 mL of 40% HF solution in a polytetrafluoroethylene container. The mixture was centrifuged (3,000 rpm, 5 min), and the resulting precipitate was rinsed with deionized water to a near-neutral supernatant pH. Finally, vacuum drying at 60 °C for 12 h yielded MXene powder.

Preparation of Ti_3C_2-TPAL

Ti_3C_2-NH_2 was obtained by treating 300 mL of MXene dispersion (10 mg mL^{-1}) with 2 g of NH_4F under argon at 60 °C for 12 h. After thorough rinsing, the obtained Ti_3C_2-NH_2 was vacuum-dried at 60 °C for 8 h. The dried Ti_3C_2-NH_2 was then dispersed at 20 mg mL^{-1} and mixed with TPAL solution at 5 mg mL^{-1}. 10 mL of Ti_3C_2-NH_2 dispersion (20 mg mL^{-1}) was mixed with 20 mL of TPAL solution (5 mg mL^{-1}), corresponding to feeding masses of 200 mg for Ti_3C_2-NH_2 and 100 mg for TPAL. The mixture was stirred at 50 °C and 300 rpm for 12 h to promote dehydration condensation. After centrifugation, the obtained Ti_3C_2-TPAL was washed repeatedly until the supernatant reached neutral pH to remove excess unreacted TPAL, followed by vacuum drying at 60 °C for 8 h.

Materials characterization

Field-emission scanning electron microscopy (FE-SEM, Hitachi SU8220) and high-resolution transmission electron microscopy (HRTEM, JEOL JEM-2100F) were employed to characterize the morphology and structure of the samples. Phase information was obtained from XRD measurements performed on a Shimadzu XRD-6100 diffractometer with Cu Kα radiation (λ = 1.5406 Å). Surface elemental composition and chemical states were investigated using X-ray photoelectron spectroscopy (XPS, Thermo Scientific K-Alpha, Al Kα source). Fourier-transform infrared spectroscopy (FTIR, Thermo Scientific Nicolet iS5) was conducted to identify surface functional groups and bonding characteristics. The zeta potential of the samples dispersed in aqueous media was measured at 25 °C using a Malvern Zetasizer Nano ZS90 to evaluate surface charge behavior and colloidal dispersion stability. N_2 adsorption-desorption isotherms (Micromeritics ASAP 2460) were measured to obtain the Brunauer-Emmett-Teller (BET) specific surface area and pore-size distribution. The samples were degassed under vacuum at 120 °C for 8 h before testing.

Electrochemical measurements

Working electrodes were fabricated by mixing the active material, poly(vinylidene fluoride) (PVDF), and carbon black in N-methyl-2-pyrrolidone (99.9%) at a mass ratio of 80:10:10. After 6 h of stirring, the slurry was cast onto Cu foil and vacuum-dried at 80 °C for 12 h, yielding a Ti_3C_2-TPAL mass loading of about 1.5 mg cm^{-2}. CR2032 coin-type half cells were assembled in a high-purity Ar-filled glovebox. Sodium metal served as both the counter and reference electrode, while Whatman GF/F glass fiber was used as the separator. The electrolyte was 1 M $NaPF_6$ dissolved in diethylene glycol dimethyl ether.

Full cells employing a Ti_3C_2-TPAL anode and an NFPP cathode were assembled. For the full-cell assembly, the cathode was prepared by coating a slurry composed of sodium iron pyrophosphate (NFPP), carbon black, and PVDF (80:10:10 weight ratio) onto Al foil. For full-cell assembly, Ti_3C_2-TPAL anodes were first pre-activated in Na-metal half cells for 10 cycles and then charged to 2.5 V *vs.* Na/Na^+ to obtain a desodiated state. The cells were disassembled in an Ar-filled glovebox without air exposure. The pre-activated anodes were not washed. Excess electrolyte on the electrode surface was gently removed using clean filter paper before assembling the Ti_3C_2-TPAL||NFPP full cells. This pre-activation step was used to form a relatively stable SEI on the Ti_3C_2-TPAL anode and reduce the influence of irreversible reactions during the initial full-cell cycling. By fixing the charge and discharge cut-off potentials of the NFPP cathode at 4.0 and 2.0 V, respectively, the full-cell operating window was determined to be 0.04-3.65 V. To ensure the cathode limited the energy density, the areal mass loadings were balanced at ~1.5 mg cm^{-2} for Ti_3C_2-TPAL and ~1.3 mg cm^{-2} for NFPP. Electrolyte and separator configurations matched those used in half-cell measurements.

Cyclic voltammetry (CV) and electrochemical impedance spectroscopy (EIS) measurements were performed. The tests were conducted on a CHI660E electrochemical workstation. For EIS, spectra were collected between 100 kHz and 0.1 Hz. Galvanostatic cycling was performed using a LAND CT3004A battery tester. Galvanostatic intermittent titration technique (GITT) measurements were also conducted on the same equipment. During the GITT measurement, the cell was subjected to a galvanostatic pulse of 0.1 A g^{-1} for 600 s, followed by an open-circuit rest for 3,600 s to allow the system to reach electrochemical equilibrium.

The gravimetric energy density (E, Wh kg^{-1}) was obtained by integrating the discharge voltage against specific capacity[29]:

$$E = \int V dQ \tag{1}$$

where Q (mAh g^{-1}) denotes the discharge specific capacity and V (V) represents the instantaneous cell voltage during discharge. The power density was calculated based on the energy density and the total discharge time[30]:

$$P = E/t \tag{2}$$

where t (h) is the duration of the discharge process.

DFT calculations

All DFT calculations were performed using the Vienna Ab initio Simulation Package (VASP). The exchange-correlation interactions were treated using the Perdew-Burke-Ernzerhof (PBE) functional within the generalized gradient approximation (GGA). The projector augmented wave (PAW) method was used to describe electron-ion interactions, and the plane-wave cutoff energy was set to 520 eV. The optimized structures were obtained when the energy variation was below 10^{-5} eV and the atomic forces were smaller than 0.02 eV $Å^{-1}$. The adsorption energy (E_a) for Na adsorption on the sample surface was defined as

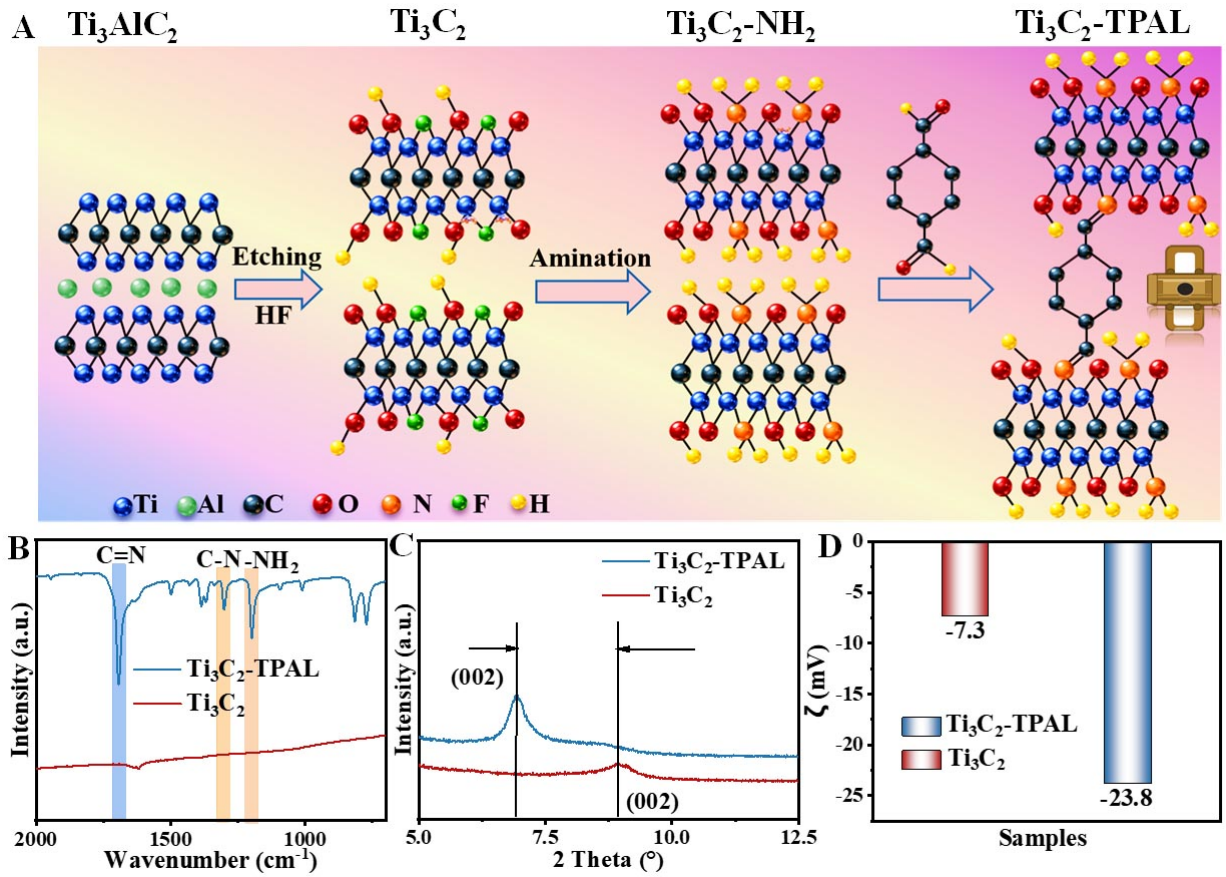

Figure 1. (A) Schematic of the preparation of Ti_3C_2-TPAL. (B) FTIR spectra, (C) XRD patterns, and (D) zeta potentials of Ti_3C_2-TPAL and Ti_3C_2.

follows[31]:

$$E_a = (E_{Na+samples} - E_{samples} - E_{Na}) \quad (3)$$

In this equation, $E_{Na+samples}$, $E_{samples}$, and E_{Na} correspond to the total energies of the Na-adsorbed system, the clean substrate, and the bulk Na reference, respectively. To analyze the migration kinetics of Na^+ ions, the climbing image nudged elastic band (CI-NEB) method was used to map out the minimum energy paths (MEPs) and identify transition states.

RESULTS AND DISCUSSION

The preparation route of Ti_3C_2-TPAL is illustrated in Figure 1A. Ti_3C_2 MXene was first obtained by treating the Ti_3AlC_2 precursor with HF, which selectively extracted Al from the MAX structure [Supplementary Figure 1]. Subsequently, amino groups ($-NH_2$) were introduced via ammonium fluoride (NH_4F) grafting reaction to obtain the functionalized intermediate Ti_3C_2-NH_2. Finally, Ti_3C_2-TPAL composite was constructed by the covalent coupling of Ti_3C_2-NH_2 and TPAL via a dehydration condensation reaction. In this structure, TPAL provides two coupled structural functions: covalent imine anchoring and rigid interlayer pillaring. These two effects suppress sheet restacking and stabilize the expanded Ti_3C_2 galleries, thereby improving the accessibility of Na^+ storage sites.

The FTIR spectrum in Figure 1B shows that, compared with pristine Ti_3C_2, Ti_3C_2-TPAL exhibits characteristic peaks assigned to C=N (1,693.5 cm^{-1}), C-N (1,301.2 cm^{-1}), and amino-related vibrations, $-NH_2$ (1,198.3 cm^{-1})[32], supporting the successful introduction of TPAL and the formation of imine-related bonding

structures. To further distinguish chemical grafting from simple physical mixing, FTIR spectra of Ti_3C_2, Ti_3C_2-NH_2, and the Ti_3C_2-NH_2/TPAL physical mixture were added in Supplementary Figure 2. The physical mixture retains the amino-related vibration features of Ti_3C_2-NH_2, indicating that simple mixing does not lead to an obvious condensation reaction, further supporting the formation of imine-related bonding structures in Ti_3C_2-TPAL. XRD analysis was used to examine the structural evolution induced by TPAL grafting. The (002) reflection shifts from 8.9° for pristine Ti_3C_2 to 6.9° for Ti_3C_2-TPAL, confirming the enlargement of the average distance between layers, which creates more pathways for Na^+ transport between MXene layers [Figure 1C].

Ti_3C_2-TPAL exhibits a zeta potential of -23.8 mV [Figure 1D], whereas that of Ti_3C_2 is only -7.3 mV, indicating that the grafting of organic molecules increases the electronegativity of Ti_3C_2-TPAL. In electrolytes, Na^+ ions are usually accompanied by a solvation sheath (surrounded by solvent molecules). To intercalate into the electrode material, Na^+ ions must first shed these solvent molecules (desolvation), which is typically an energy-consuming and slow process. A strongly negatively charged surface can directly undergo electrostatic adsorption with bare Na^+ ions, aiding in stripping solvent molecules and thereby accelerating interfacial reaction kinetics. In other words, grafting TPAL not only acts as a "pillar" in the Ti_3C_2 interlayers to expand the spacing but also significantly increases the electronegativity of Ti_3C_2. Analogous to acceleration devices on a widened highway, the negatively charged functional groups within the expanded interlayer spacing synergistically promote rapid Na^+ ions migration and strong adsorption.

The morphological changes induced by TPAL modification were further investigated by SEM and transmission electron microscopy (TEM). The results show that the Ti_3C_2-TPAL composite completely inherits the 3D layered framework of Ti_3C_2 [Figure 2A and B]. As evidenced by HRTEM images [Figure 2C and D], the local interlayer distance of Ti_3C_2-TPAL is approximately 1.41 nm, larger than that of pristine Ti_3C_2 (0.90 nm). Since HRTEM reflects only selected local regions, the average interlayer spacing was further evaluated from the XRD (002) peak using Bragg's law. The (002) peak shifts from 8.9° for Ti_3C_2 to 6.9° for Ti_3C_2-TPAL, corresponding to calculated d-spacings of 0.993 and 1.280 nm, respectively. This decrease in the (002) diffraction angle confirms the enlarged average interlayer spacing after TPAL grafting. Additional control data show that Ti_3C_2-NH_2 has a (002) peak at 8.19° with a d-spacing of approximately 1.08 nm, whereas the Ti_3C_2-NH_2/TPAL physical mixture shows a (002) peak at 8.58° with a d-spacing of approximately 1.03 nm [Supplementary Figures 3 and 4], indicating that simple mechanical mixing with TPAL does not induce obvious interlayer expansion. These XRD-derived average spacings are consistent with the HRTEM observation, confirming the expanded interlayer structure after TPAL grafting. This widened spacing provides more accessible pathways for Na^+ transport and interfacial storage, while reducing ion-diffusion resistance within the expanded Ti_3C_2 galleries. Additionally, SEM-energy-dispersive X-ray spectroscopy (EDX) elemental mapping [Figure 2E] confirms the uniform distribution of C, N, and Ti elements in Ti_3C_2-TPAL, indicating the homogeneous incorporation of N-containing amino/imine-related species after TPAL grafting. Based on EDX atomic-percentage analysis, the mass fraction of covalently grafted TPAL is estimated to be ~16.9 wt%, and full calculation details are retained in Supplementary Figure 5 .

The surface composition, valence states, and bonding environment of the composite were further analyzed by XPS. After TPAL grafting, no pronounced shift was observed in the main Ti 2p or O 1s peaks, suggesting that the Ti-C framework and oxygen-containing surface terminations of Ti_3C_2 were largely preserved. The main XPS changes are reflected in the N 1s and C 1s regions, where the C=N and C-N components confirm the formation of imine-related bonding structures between TPAL and aminated Ti_3C_2. As shown in

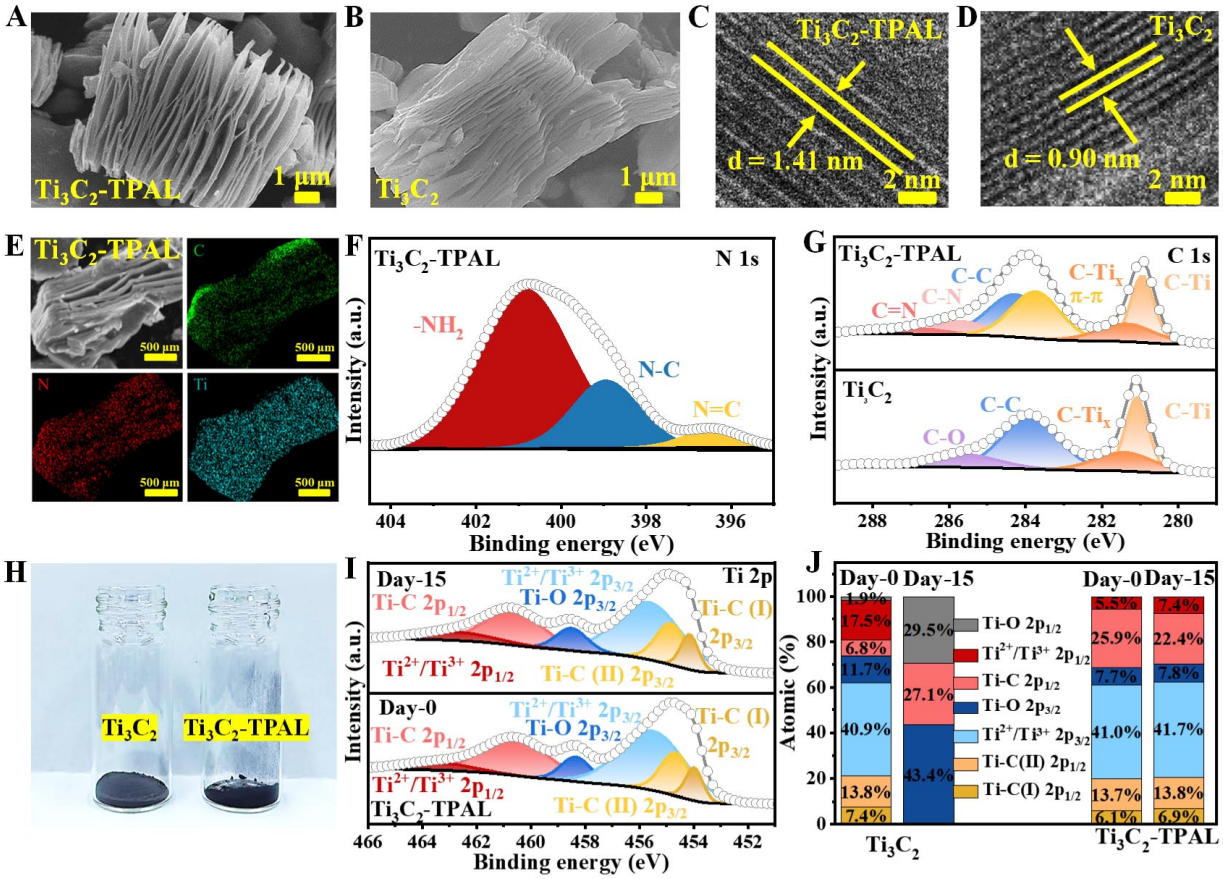

Figure 2. SEM images of (A) Ti_3C_2-TPAL and (B) Ti_3C_2. HRTEM images of (C) Ti_3C_2-TPAL and (D) Ti_3C_2. (E) SEM image and elemental mappings of Ti_3C_2-TPAL. High-resolution XPS spectra of Ti_3C_2-TPAL in the (F) N 1s and (G) C 1s regions. (H) Digital photographs of Ti_3C_2 and Ti_3C_2-TPAL after aging under ambient conditions. (I) Fitted Ti 2p XPS spectra and (J) relative atomic percentages of Ti species derived from Ti 2p fitting for Ti_3C_2 and Ti_3C_2-TPAL before and after aging.

Figure 2F, N 1s deconvolution gives three fitted components located at 396.4, 398.9, and 400.9 eV[33-35], corresponding to C=N, C-N, and -NH_2 configurations. These peaks reveal the formation of robust chemical bonds between the surface-aminated Ti_3C_2 and TPAL molecules. A further comparison of C 1s spectra [Figure 2G] shows that Ti_3C_2-TPAL exhibits characteristic peaks of π-π* transitions, C-N, and C=N at 283.7, 285.7, and 287.0 eV[36,37], respectively, which are absent in pristine Ti_3C_2. This significant signal evolution further corroborates the introduction of TPAL.

The resistance of Ti_3C_2-TPAL against ambient oxidation was preliminarily evaluated by comparing the color, morphology, and Ti 2p XPS spectra of Ti_3C_2 and Ti_3C_2-TPAL after exposure to the same air-aging conditions. Air aging experiments indicate that Ti_3C_2-TPAL maintains its original black color and intact 3D layered microscopic skeleton after 15 days of environmental exposure [Figure 2H, Supplementary Figure 6]; in contrast, pristine Ti_3C_2 not only faded to grayish-black but also saw its layered structure collapse due to oxidation, making the accordion structure unrecognizable. The relative content of the Ti-O $2p_{3/2}$ peak in the high-resolution Ti 2p spectrum serves as a key indicator for evaluating the oxidation degree of the Ti_3C_2 surface. Analysis shows that the Ti-O $2p_{3/2}$ content of aged Ti_3C_2-TPAL only slightly increased from 7.7 at% to 7.8 at% [Figure 2I and J]. Conversely, this component in pristine Ti_3C_2 surged from 11.7 at% to 43.4 at%, confirming deep oxidative destruction of its crystal structure. This comparison indicates that TPAL grafting

can mitigate the oxidation of Ti_3C_2 under the present ambient exposure conditions, which may help preserve surface-active sites during short-term storage. The porous characteristics of Ti_3C_2 and Ti_3C_2-TPAL were further evaluated by N_2 adsorption-desorption measurements [Supplementary Figure 7]. The BET surface area increases from 7.9354 $m^2 g^{-1}$ for pristine Ti_3C_2 to 37.3411 $m^2 g^{-1}$ for Ti_3C_2-TPAL, indicating that TPAL grafting improves the accessible surface area of the layered MXene structure. The corresponding pore-size distribution further shows a more pronounced pore-volume contribution in Ti_3C_2-TPAL, suggesting improved electrolyte-accessible channels after molecular grafting. These features can enhance electrolyte access and accelerate Na^+ transport across the expanded MXene interlayers.

The Na-storage properties of Ti_3C_2-TPAL were examined in SIB half-cells over 0.01-2.5 V. The first three CV curves collected at 0.1 mV s^{-1} are shown in Figure 3A. In the first CV curve, the reduction current below 1.5 V can be mainly attributed to SEI formation, electrolyte decomposition, and irreversible surface/interfacial reactions associated with Na^+ storage. Figure 3B shows that Ti_3C_2-TPAL delivers 385.8 mAh g^{-1} during the first discharge and 153.9 mAh g^{-1} during the subsequent charge at 0.1 A g^{-1}. The relatively low initial Coulombic efficiency is a common issue for MXene-based sodium-storage anodes, mainly due to their abundant surface terminations, large exposed surface area, and defect-rich layered structure. This irreversible capacity loss can be attributed to SEI formation, electrolyte decomposition, irreversible reactions involving surface functional groups, and partial Na^+ trapping at defects or interlayer sites. Therefore, Ti_3C_2-TPAL should be regarded as a MXene-based anode with improved high-rate stability and long-term cycling durability, while its initial Coulombic efficiency still requires further optimization. The nearly identical CV and charge-discharge profiles from the second to third cycle reflect good reaction reversibility. During cycling at 0.1 A g^{-1}, Ti_3C_2-TPAL maintains 88.1 mAh g^{-1} after 200 cycles [Supplementary Figure 8], whereas pristine Ti_3C_2 only delivers 55.7 mAh g^{-1}. The higher capacity retention supports the role of TPAL grafting in reinforcing the electrode framework and improving cycling stability.

Rate performance tests show that Ti_3C_2-TPAL delivers excellent high-rate capacities of 101.9, 91.1, 81.7, 74.9, 67.6, and 57.0 mAh g^{-1} at 0.2, 0.5, 1, 2, 5, and 10 A g^{-1} [Figure 3C], respectively, far exceeding those of the Ti_3C_2 anode. After the current density returns to 0.2 A g^{-1}, the capacity recovers to 90.8 mAh g^{-1}, indicating excellent rate and reversibility for Ti_3C_2-TPAL. Even after 2,500 cycles under a rate of 5 A g^{-1}, a capacity of 54.3 mAh g^{-1} is preserved [Figure 3D], demonstrating the excellent long-cycling performance. For comparison, the long-term cycling performances of pristine Ti_3C_2 and Ti_3C_2-NH_2 were further tested under the same current density and are provided in Supplementary Figure 9. Both control samples show lower capacities than Ti_3C_2-TPAL after long-term cycling, indicating that TPAL grafting provides additional structural stabilization beyond pristine Ti_3C_2 and the aminated intermediate. The rate capability and long-term cycling stability of Ti_3C_2-TPAL compare favorably with those of recently reported MXene-based anodes. [Figure 3E, Supplementary Table 1].

Electrochemical kinetic analysis further elucidates the impact of the imine-bond-based covalent anchoring between TPAL and Ti_3C_2 on optimizing battery performance. The CV curves exhibit similar shapes at scan rates from 0.2 to 1.1 mV s^{-1} [Supplementary Figure 10]. Despite minor peak shifts, the consistent shapes confirm a stable electrochemical mechanism. Compared to Ti_3C_2, the CV curves of Ti_3C_2-TPAL exhibit reduced polarization effects and enhanced reversibility. Furthermore, based on the relationship between the response current (i) and the scan rate (v)[38]:

$$i = av^b \tag{4}$$

The b value is commonly used to distinguish diffusion-limited and surface-capacitive behaviors, with values approaching 1.0 indicating a stronger capacitive response. As shown in Figure 3F, Ti_3C_2-TPAL exhibits b

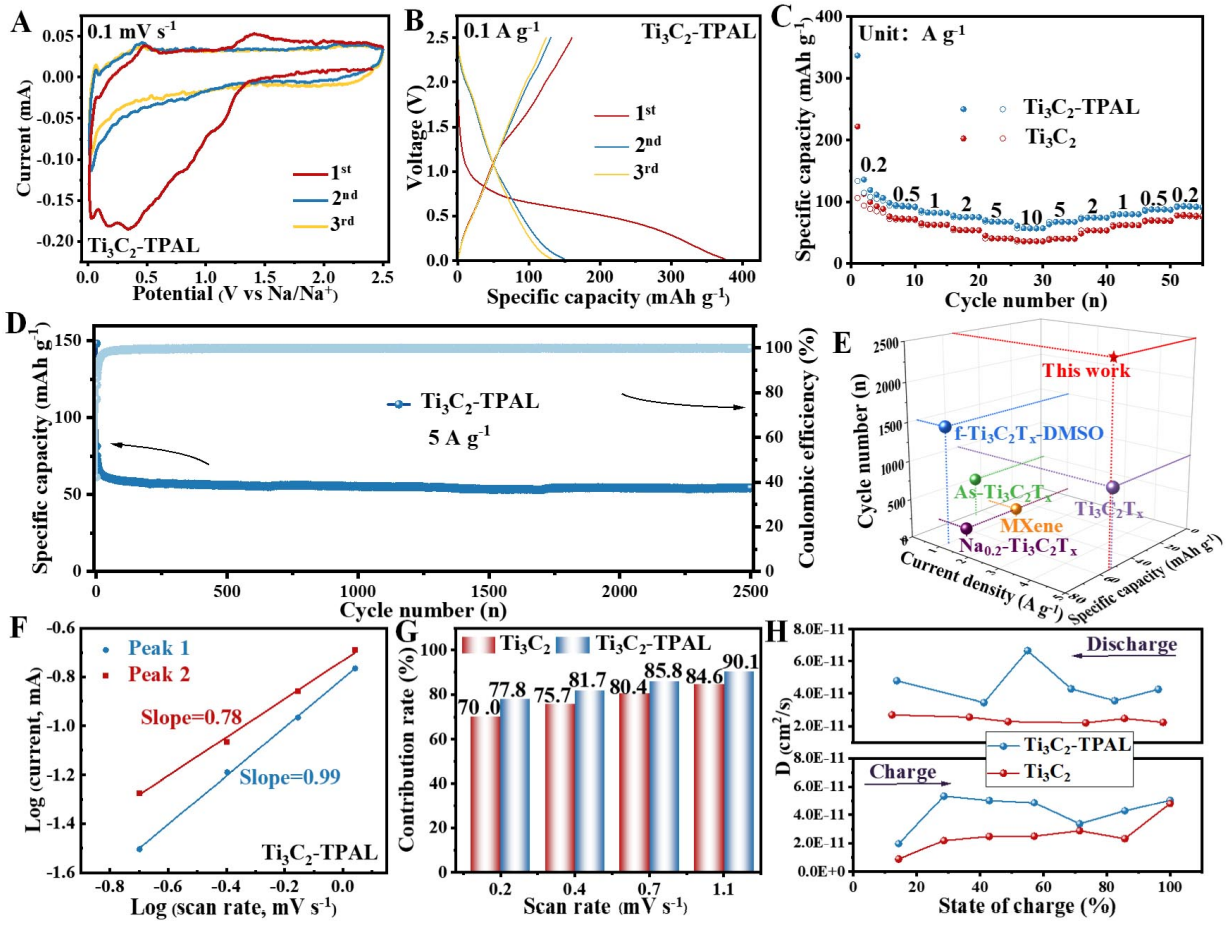

Figure 3. (A) CV curves recorded at a scan rate of 0.1 mV s^{-1}, (B) galvanostatic charge-discharge plots tested at 0.1 A g^{-1}, (C) rate capability under different current densities, and (D) long-cycle durability at 5 A g^{-1} of Ti_3C_2-TPAL. (E) Performance comparison with previously reported MXene-based anodes. (F) Relationship between peak current and scan rate of Ti_3C_2-TPAL. (G) Capacitive contribution fractions and (H) Na^+ diffusion coefficients of Ti_3C_2-TPAL and Ti_3C_2.

values of 0.99 and 0.78 for peak 1 and peak 2, respectively, which exceed those of pristine Ti_3C_2 (0.78 and 0.76). This comparison reveals that Na^+ storage in Ti_3C_2-TPAL is mainly governed by surface-controlled pseudocapacitive processes. The pseudocapacitive-dominated Ti_3C_2-TPAL electrode enables fast Na^+ uptake and release, thereby supporting its favorable high-rate response. The capacity fractions from capacitive and diffusion-limited processes were further quantified using[38]:

$$i = k_1 v + k_2 v^{1/2} \tag{5}$$

Here, $k_1 v$ and $k_2 v^{1/2}$ correspond to the surface-capacitive and diffusion-limited components, respectively. As presented in Figure 3G, the surface-capacitive fraction of Ti_3C_2-TPAL is 77.8% at 0.2 mV s^{-1} and rises to 90.1% as the scan rate reaches 1.1 mV s^{-1}. This value is higher than that of pristine Ti_3C_2 under the same scan rate (84.6%), indicating faster surface-dominated Na^+ storage kinetics after TPAL grafting. These kinetic results indicate that the Na-storage behavior of Ti_3C_2-TPAL is mainly governed by surface-controlled pseudocapacitive processes rather than typical bulk intercalation. Therefore, the capacity contribution is attributed primarily to fast Na^+ adsorption/desorption at accessible surfaces and interfaces, assisted by limited Na^+ insertion within the expanded Ti_3C_2 galleries. GITT tests show that Ti_3C_2-TPAL possesses higher

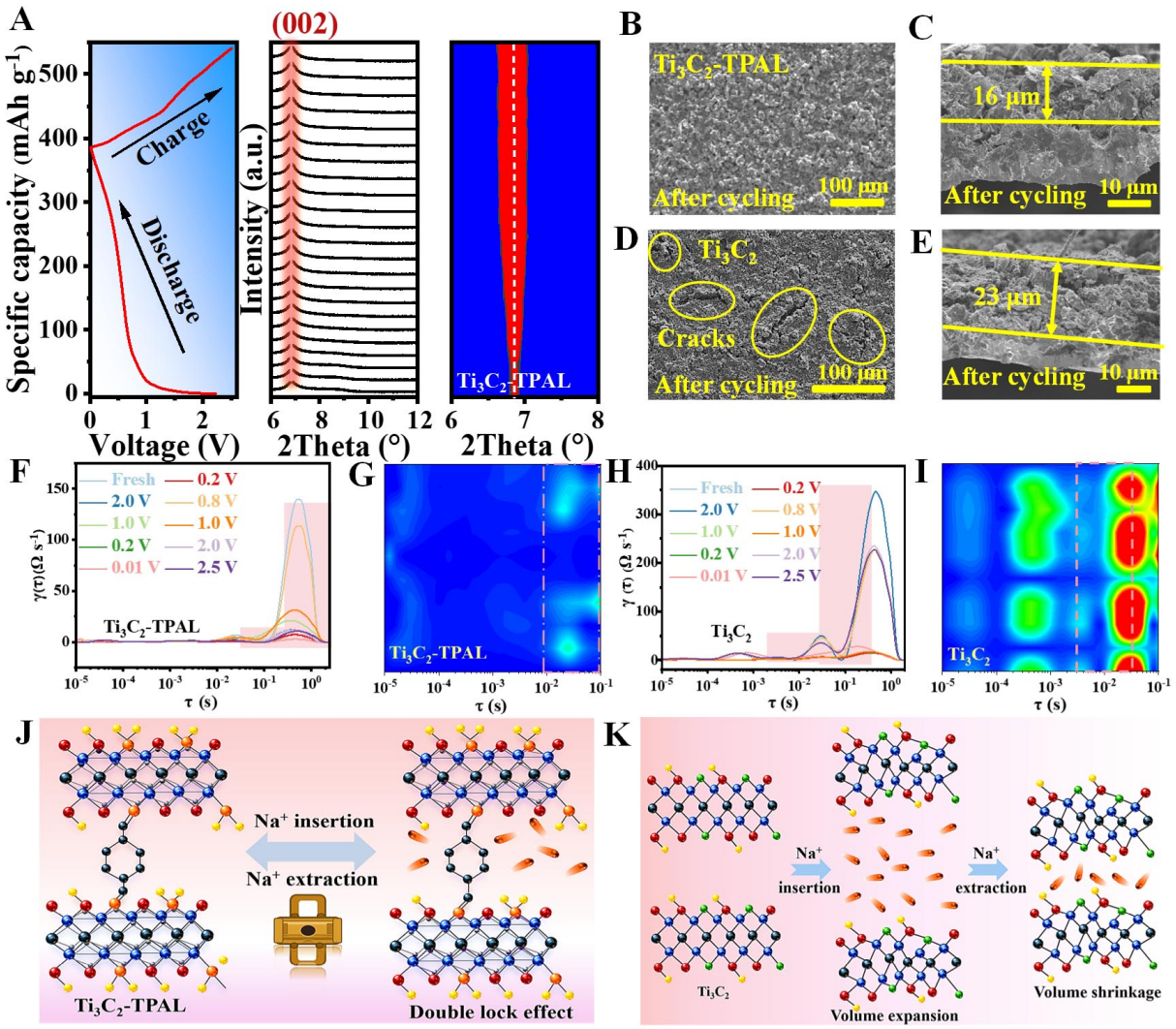

Figure 4. (A) Time-resolved *in situ* XRD results obtained when Ti_3C_2-TPAL undergoes sodiation and desodiation. SEM images of cycled (B and C) Ti_3C_2-TPAL and (D and E) Ti_3C_2 electrodes. DRT analysis of (F and G) Ti_3C_2-TPAL and (H and I) Ti_3C_2 during charge and discharge. Schematic illustrations of Na^+ storage mechanisms in (J) Ti_3C_2-TPAL and (K) Ti_3C_2.

diffusion coefficients during both charge and discharge processes [Figure 3H, Supplementary Figure 11]. Electrochemical kinetic test results indicate that grafting TPAL molecules increases reactive active sites and significantly boosts reaction kinetics. Functioning as rigid pillars, TPAL expands the Ti_3C_2 interlayer spacing to facilitate ion transport and minimize diffusion resistance. This synergistic effect effectively promotes the rapid and stable storage of Na^+ ions.

In situ XRD and SEM were further utilized to verify the structural stability of Ti_3C_2-TPAL. Interestingly, the (002) characteristic peak of Ti_3C_2-TPAL remains stable at 6.9° during the charge-discharge process [Figure 4A], with almost no shift observed. In contrast, the (002) reflection of pristine Ti_3C_2 shifts from 8.9° to 8.3° during discharge [Supplementary Figure 12]. After the subsequent charge process, this peak only recovers to 8.4° rather than returning to its initial position, suggesting incomplete structural recovery and irreversible lattice distortion during cycling. This breathing phenomenon of Ti_3C_2 has been widely reported in many research works[39,40].

After prolonged cycling, Ti_3C_2-TPAL preserves a smooth and compact electrode surface comparable to the pristine state [Figure 4B, Supplementary Figure 13]. The electrode thickness changes moderately from 12 to 16 μm [Figure 4C], corresponding to a thickness increase of 33.3%. The moderate thickness increase of Ti_3C_2-TPAL after cycling may be mainly associated with SEI formation. By comparison, the cycled pristine Ti_3C_2 electrode shows pronounced surface cracking [Figure 4D], with its thickness increasing from 14 to 23 μm [Figure 4E], corresponding to a thickness expansion of 64.3%. The continuous expansion and contraction of Ti_3C_2 interlayer spacing are considered the main cause of Ti_3C_2 agglomeration or electrode cracks, which subsequently lead to cycling performance degradation.

DRT analysis allowed for resolving the EIS spectra into distinguishable relaxation processes [Supplementary Figures 14 and 15]. DRT analysis was used as a complementary method to separate overlapping relaxation processes in the EIS spectra. Because the extracted DRT peaks can be influenced by regularization and data quality, the peak assignment is discussed cautiously and mainly used for comparative analysis between Ti_3C_2 and Ti_3C_2-TPAL under the same processing conditions. Within the DRT spectrum, distinct peaks are assigned to specific physicochemical processes. According to the commonly used interpretation of DRT spectra for battery electrodes, the relaxation peaks in the 0.01-0.1 s region are tentatively assigned to interfacial charge-transfer-related processes. This assignment should be regarded as a comparative interpretation rather than an exclusive identification, because DRT peak positions can be affected by data quality, regularization parameters, and overlapping electrochemical processes. The relaxation signals appearing at τ values above 0.1 s can be assigned to electrolyte-phase mass-transport processes.

The charge-transfer time constant of Ti_3C_2-TPAL remains nearly unchanged at 0.020-0.025 s during charge and discharge [Figure 4F and G], which is lower than the 0.029-0.032 s of pristine Ti_3C_2 [Figure 4H and I]. This result confirms that the introduction of TPAL molecules lowers the charge transfer barrier, as schematically illustrated in Figure 4J and K. Furthermore, the DRT intensity plot can further reveal the stability of the electrode over long-term cycling. Compared to Ti_3C_2, the DRT intensity of Ti_3C_2-TPAL varies less during cycling [Supplementary Figure 15], highlighting the electrochemical stability of Ti_3C_2-TPAL. This not only corroborates the anchoring effect of TPAL on Ti_3C_2 sheets but also effectively inhibits structural accumulation and collapse. The stability of TPAL molecules during long-term cycling was also considered. Although partial cleavage of imine-related bonds cannot be completely excluded during repeated sodiation/desodiation, the stable long-term cycling behavior, nearly unchanged (002) peak position during *in situ* XRD measurements, reduced electrode deformation after cycling, and relatively stable DRT response suggest that the TPAL-assisted interlayer structure is largely maintained during cycling. Possible local bond cleavage or interfacial side reactions may still occur and should be further clarified by post-cycling spectroscopic analysis in future work. The Ti_3C_2-TPAL electrode demonstrates a unique "double-lock" effect: Based on the above structural and electrochemical evidence, the double-lock effect of TPAL can be assigned to covalent anchoring and interlayer pillaring. The covalent imine linkages restrict the restacking and slippage of Ti_3C_2 sheets, while the rigid aromatic TPAL pillars stabilize the enlarged interlayer spacing. This assignment is supported by the chemical-bonding evidence from FTIR/XPS, the enlarged interlayer spacing from XRD and HRTEM, the nearly unchanged (002) peak position during *in situ* XRD measurements, and the reduced electrode deformation after cycling. Therefore, the double-lock architecture contributes to the improved structural integrity and high-rate sodium-storage kinetics of Ti_3C_2-TPAL.

To provide trend-level theoretical insight into the possible influence of TPAL grafting on Na adsorption and migration, simplified DFT calculations were performed. It should be noted that the DFT models used here are simplified representations of Ti_3C_2 and Ti_3C_2-TPAL. Real $Ti_3C_2T_x$ MXenes contain mixed surface terminations, such as -O, -OH, and -F, which may affect Na adsorption, diffusion barriers, electronic

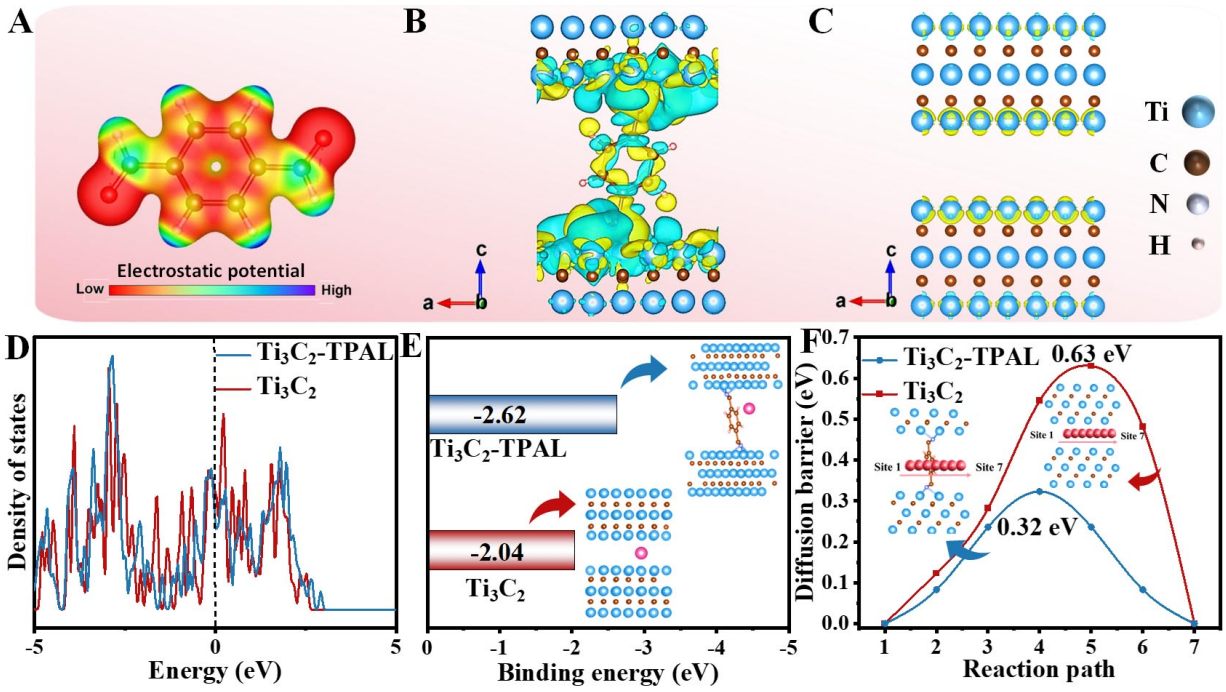

Figure 5. (A) The electrostatic potential layout calculated for TPAL molecule. Charge-density-difference maps of (B) Ti_3C_2-TPAL and (C) Ti_3C_2. (D) DOS profiles, (E) Na adsorption energies, and (F) migration energy barriers of Ti_3C_2-TPAL and Ti_3C_2.

structure, and interlayer spacing. Therefore, the DFT results are used as auxiliary evidence rather than a complete description of the real $Ti_3C_2T_x$ surface chemistry. Theoretical calculations indicate significant negative charge regions on the TPAL molecule surface [Figure 5A]. This feature enhances the electrostatic adsorption of Na^+ ions, thereby suggesting potential active sites for Na^+ storage within the Ti_3C_2-TPAL composite. Zeta potential test results further validate this theoretical prediction. The charge-density-difference maps are illustrated in Figure 5B and C. In these maps, electron-rich regions are shown in yellow, while electron-deficient regions are displayed in blue. Compared with the nearly uniform charge distribution on pristine Ti_3C_2, Ti_3C_2-TPAL exhibits more evident interfacial charge redistribution, suggesting modified local electronic interactions after TPAL grafting. The charge-density-difference maps suggest that TPAL grafting induces local interfacial charge redistribution rather than a uniform charge distribution. This interfacial polarization may contribute to improved Na^+ affinity and charge-transfer behavior.

In addition, density of states analysis indicates [Supplementary Figure 16] that Ti_3C_2-TPAL presents a continuous density of states at the Fermi level [Figure 5D]. The absence of a significant band gap indicates excellent electronic conductivity, ensuring superior electron transport efficiency and providing a guarantee for the optimization of Na^+ ions storage kinetics. Adsorption energy calculation results [Figure 5E, Supplementary Figure 17] indicate that the Na^+ ions adsorption energy of Ti_3C_2-TPAL is -2.62 eV, which is significantly lower than the -2.04 eV of Ti_3C_2. Lower adsorption energy implies a stronger and more stable adsorption effect of the material surface on Na^+ ions, which can supply sufficient ion sources for the Na^+ ions storage process. Na^+ ions diffusion barrier calculation [Figure 5F, Supplementary Figure 18] shows that the Na^+ ions diffusion barrier of Ti_3C_2-TPAL is only 0.32 eV, representing a reduction of ~49% compared to that of Ti_3C_2 (0.63 eV). The lower diffusion barrier can effectively reduce energy loss during Na^+ ions diffusion, further confirming its excellent Na^+ ions diffusion kinetics. The more negative Na adsorption energy of Ti_3C_2-TPAL indicates enhanced Na affinity and improved interfacial Na capture compared with pristine Ti_3C_2. However, stronger Na adsorption is not necessarily always beneficial, because excessively strong Na binding may restrict Na^+ migration or induce irreversible Na trapping. Therefore, the adsorption energy

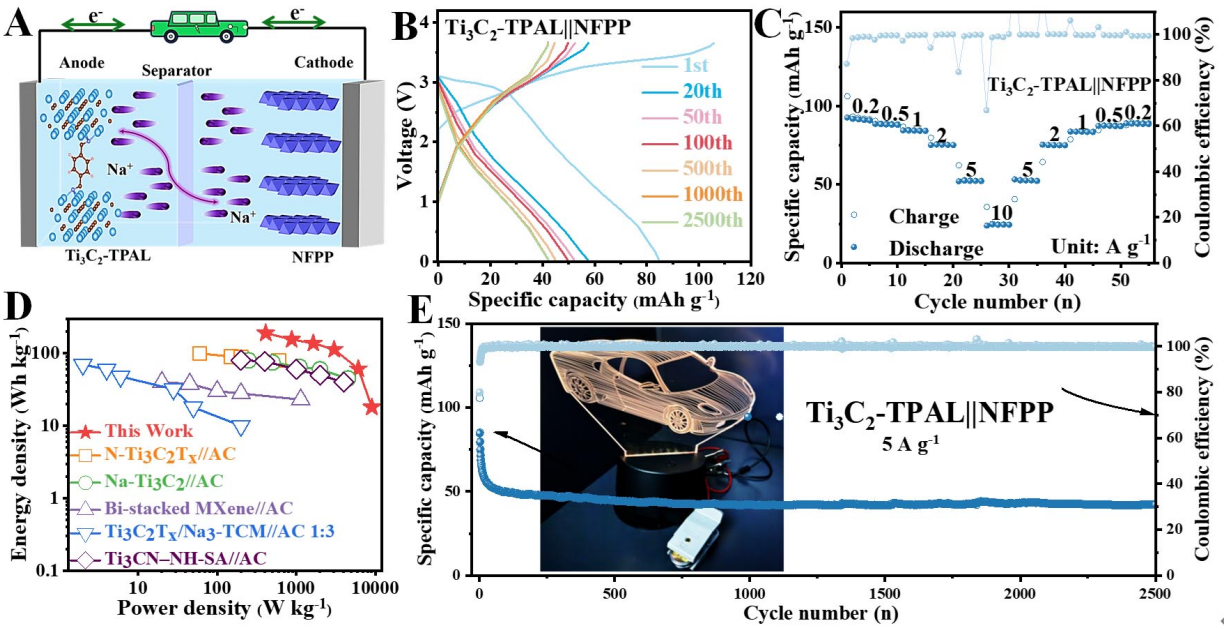

Figure 6. (A) Schematic illustration, (B) GCD profiles at 5 A g^{-1}, and (C) rate capability of the Ti_3C_2-TPAL||NFPP full cell. (D) Ragone plot compared with reported full cells. (E) Long-term cycling stability of the Ti_3C_2-TPAL||NFPP full cell at 5 A g^{-1}. Digital camera photograph of an LED powered by the full cell (Inset).

should be considered together with the Na diffusion barrier. In the present simplified model, Ti_3C_2-TPAL shows both stronger Na adsorption and a lower diffusion barrier than Ti_3C_2, suggesting that TPAL-related interfacial regulation may improve Na^+ capture without severely hindering Na^+ transport. The Ti_3C_2-TPAL composite effectively promotes the improvement of electrochemical kinetics during the Na^+ ions storage process through multi-dimensional synergistic mechanisms, including constructing abundant electronegative sites, abundant built-in electric fields, excellent electronic conductivity, and strengthening Na^+ ions adsorption while weakening its diffusion barrier.

To systematically evaluate the electrochemical performance of Ti_3C_2-TPAL in practical applications, it was matched with NFPP cathode to construct a SIBs full battery system (Ti_3C_2-TPAL||NFPP, Figure 6A). Based on the half-cell voltage profiles of NFPP and Ti_3C_2-TPAL, the Ti_3C_2-TPAL||NFPP full cell was operated within 0.04-3.65 V [Supplementary Figure 19]. The full-cell capacity obtained in this work, together with energy and power densities, was normalized to the active material of the NFPP cathode. Under 5 A g^{-1}, the initial charge and subsequent discharge capacities are 105.7 and 84.6 mAh g^{-1}, respectively, corresponding to an initial Coulombic efficiency of 80.0% [Figure 6B]. Furthermore, the full battery also presents excellent rate performance. At current densities of 0.2, 0.5, 1, 2, 5, and 10 A g^{-1} [Figure 6C], the discharge specific capacities are 90.8, 88.4, 84.2, 75.2, 52.3, and 24.5 mAh g^{-1}, respectively. When the current density recovers to 0.2 A g^{-1}, the specific capacity can still reach 88.8 mAh g^{-1}. Correspondingly, the Ti_3C_2-TPAL||NFPP full cell delivers a maximum energy density of 190.8 Wh kg^{-1} and a power density of 9,040 W kg^{-1} based on the NFPP cathode active mass, demonstrating competitive energy-power output among reported MXene-based full cells [Figure 6D, Supplementary Table 2]. Even after 2,500 cycles at 5 A g^{-1}, the cell still provides 42.2 mAh g^{-1} and maintains nearly 100% Coulombic efficiency [Figure 6E], confirming its durable full-cell operation. The long-term cycling stability of the Ti_3C_2-TPAL||NFPP full cell can be attributed to the stabilized Ti_3C_2-TPAL anode structure and the stable Na^+ supply from the NFPP cathode. The TPAL-induced covalent anchoring and interlayer pillaring help suppress MXene restacking and mitigate structural deformation during repeated cycling, thereby maintaining stable Na-storage kinetics. A light-emitting diode (LED) was successfully powered by the assembled full cell [Inset of Figure 6E]. High-performance SIBs show significant advantages

in smart grids, electric vehicles, and the energy storage sector. SIBs stabilize grid fluctuations and enhance renewable energy integration with cost advantages. Their fast-charging capability suits them for microcars and buses, while their safety profile supports wearable electronics. Ultimately, SIBs applications in smart grids and storage will facilitate "dual carbon" goals through technological diversification.

CONCLUSIONS

In summary, Ti_3C_2-TPAL was constructed through a molecular grafting strategy based on a well-defined double-lock architecture. The first lock originates from covalent imine anchoring between TPAL and aminated Ti_3C_2, which suppresses sheet restacking and interlayer slippage. The second lock arises from rigid aromatic TPAL pillaring, which enlarges and stabilizes the Ti_3C_2 interlayer spacing. These coupled structural effects contribute to the enhanced electrochemical performance of Ti_3C_2-TPAL, which delivers 57.0 mAh g^{-1} at 10 A g^{-1} and maintains 54.3 mAh g^{-1} after 2,500 cycles at 5 A g^{-1}, showing competitive high-rate stability among reported MXene-based sodium-storage anodes. *In situ* XRD and DRT results indicate that TPAL grafting helps stabilize the Ti_3C_2 interlayers and reduce charge-transfer resistance. Simplified DFT calculations further provide trend-level support that TPAL-related interfacial regulation may enhance Na^+ affinity and lower the Na migration barrier. Moreover, the assembled Ti_3C_2-TPAL||NFPP full battery demonstrates a cathode-mass-normalized energy density of 190.8 Wh kg^{-1} and a power density of 9,040 W kg^{-1}. Overall, this work demonstrates that TPAL grafting can improve the interlayer stability, ambient oxidation resistance, and high-rate cycling durability of Ti_3C_2-based anodes. Rather than fundamentally solving all limitations of MXene anodes, this molecular-grafting strategy provides a useful approach for regulating MXene interlayers and enhancing high-rate sodium-storage kinetics.

DECLARATIONS

Authors' contributions

Paper writing and experimental, data analysis: Huang, X.; Fei, J.; Fan, L.
DFT calculation and review, core idea, data analysis, and supervision: Bi, H.; Bayaguud, A.; Zhang, Y.
Normal analyses: Zhang, L.; Sun, X.; Zhang, J.; Wei, C.

Availability of data and materials

The data supporting the findings of this study are available within this Article and its Supplementary Materials. Further data are available from the corresponding authors upon request.

AI and AI-assisted tools statement

Not applicable.

Financial support and sponsorship

This work was supported by the National Key R&D Program of China (2023YFB2405800), National Natural Science Foundation of China (22569019), Scientific Research Start-up Fund Project of Inner Mongolia University of Technology (DC2500002533 and DC2400003366), First-Class Discipline Scientific Research Special Project (YLXKZX-NGD-002), Science and Technology Planning Project of Hohhot (2023RC-LianHeTi-5), Natural Science Foundation of Inner Mongolia Autonomous Region of China (2025MS05111, 2025QN05006, 2026QC0348, and 2026QC0362), and Student Innovation and Entrepreneurship Training Program Project of Inner Mongolia University of Technology (2026380150 and 2026381577).

Conflicts of interest

Bi, H.; Bayaguud, A.; Zhang, Y. are the Guest Editors of the Special Issue "Beyond Lithium-Ion Batteries: Materials and Mechanisms for Sustainable Energy Storage" of the journal *Energy Materials*. They were not involved in any steps of editorial processing, notably including reviewers' selection, manuscript handling and decision making, while the other authors have declared that they have no conflicts of interest.

Ethical approval and consent to participate

Not applicable.

Consent for publication

Not applicable.

Supplementary Materials

Supplementary Materials

REFERENCES

1. Mariyappan, S.; Desai, P.; Morcrette, M.; Tarascon, J. From lab to market with sustainable sodium-ion batteries. *Nat. Sustain.* **2025**, *9*, 360-71. DOI
2. Yang, P.; Wu, Z.; Wang, S.; et al. Synergetic coupling of redox-active sites on organic electrode material for robust and high-performance sodium-ion storage. *Angew. Chem. Int. Ed.* **2023**, *62*, e202311460. DOI
3. Chen, Q.; Wen, Q.; Li, C.; et al. High-compaction spherical carbon with tunable rich pore structures for efficient sodium storage. *Adv. Mater.* **2025**, *38*, e15495. DOI
4. Li, Y.; Vasileiadis, A.; Zhou, Q.; et al. Origin of fast charging in hard carbon anodes. *Nat. Energy.* **2024**, *9*, 134-42. DOI
5. Chen, M.; Xiao, P.; Yang, K.; et al. Sn anodes protected by intermetallic $FeSn_2$ layers for long-lifespan sodium-ion batteries with high initial coulombic efficiency of 93.8 %. *Angew. Chem. Int. Ed.* **2023**, *62*, e202219177. DOI
6. Chen, Z.; Li, Y.; Wang, L.; et al. Durable alloy anode for Na-ion batteries with high volumetric energy density. *Nat. Energy.* **2026**, *11*, 449-59. DOI
7. Li, Y.; Fan, X.; Wang, L.; et al. In situ-formed C-N anchors embedded into Sn-based negative electrodes for long-life Na-ion batteries. *Nat. Commun.* **2026**, *17*, 2476. DOI PubMed PMC
8. Li, M.; Li, C.; Lu, G.; et al. Manipulation of the anode interphase by multicomponent composite sodium for fast-charging and low-temperature sodium metal batteries. *Adv. Funct. Mater.* **2025**, *35*, 2422892. DOI
9. Peng, Y. H.; Wang, Y. Y.; Wang, Z. Y.; Shao, G. S.; Hou, B. H. Decoupling dual regulatory roles and mechanisms of bismuth in low-carbon-content Sn anode for fast and stable sodium storage. *Adv. Funct. Mater.* **2025**, *36*, e13942. DOI
10. Li, D.; Zhu, Y. J.; Cheng, L.; et al. A MXene modulator enabled high-loading iodine composite cathode for stable and high-energy-density Zn-I_2 battery. *Adv. Energy. Mater.* **2024**, *15*, 2404426. DOI
11. Fan, Q.; Chen, M.; Yang, Y.; et al. Unveiling the multifunctional potential of MXenes in rechargeable batteries beyond electrode active materials. *Adv. Mater.* **2025**, *37*, 2505584. DOI
12. Rostami, S.; Park, Y. H.; Yun, I.; et al. Polymer-ligand functionalized MXene and hollow silica composite anode for improved sodium-ion batteries. *Commun. Mater.* **2026**, *7*, 89. DOI
13. Zhong, Y.; Liang, W.; Lv, T.; et al. Facile One-step modification of biomass hard carbon: tailoring hierarchical microstructures for high-energy-density sodium-ion battery anode materials. *Adv. Funct. Mater.* **2026**, *36*, e75776. DOI
14. Guo, J.; Ma, G.; Liu, G.; Dai, C.; Lin, Z. Ti_2CT_x MXene cathode host for enhanced zinc-bromine battery performance. *Adv. Energy. Mater.* **2024**, *14*, 2304516. DOI
15. Zhang, P.; Wang, X.; Zhang, Y.; et al. Burgeoning silicon/MXene nanocomposites for lithium ion batteries: a review. *Adv. Funct. Mater.* **2024**, *34*, 2402307. DOI
16. Xia, J.; Lv, M.; Zhang, S.; Xing, Y.; Zhou, G. Rational design of two-dimensional MXene-based materials for lithium-sulfur batteries. *Mater. Sci. Eng. R. Rep.* **2025**, *164*, 100985. DOI
17. Lv, M.; Xia, J.; Zhang, S.; Wang, T.; Zhou, G.; Xing, Y. Multifunctional roles of MXenes in flexible lithium-sulfur batteries: mechanistic insights, computational perspectives, and future standards. *EnergyChem* **2026**, *8*, 100190. DOI
18. Naguib, M.; Kurtoglu, M.; Presser, V.; et al. Two-dimensional nanocrystals produced by exfoliation of Ti_3AlC_2. *Adv. Mater.* **2011**, *23*, 4248-53. DOI
19. Wang, X.; Wang, Y.; Ni, K.; et al. Fullerene intercalation of MXene toward super-long-cycle sodium ion storage. *Adv. Funct. Mater.* **2024**, *34*, 2400185. DOI
20. Wu, Z.; Jiang, L.; Wang, S.; et al. Electrode design and interface engineering of MXenes promote energy storage applications. *Commun. Mater.* **2026**, *7*, 147. DOI
21. Ali, H.; Al-Farraj, E. S.; Abu-Dief, A. M.; et al. Intercalation and delamination in MXene: unlocking structural evolution and functional applications. *Coord. Chem. Rev.* **2026**, *557*, 217716. DOI

22. Zong, J.; Liang, Y.; Liu, F.; et al. Effect of combination model of $MoTe_2$ and MXene layers on sodium ion storage. *Adv. Mater.* **2025**, *37*, 2503252. DOI
23. Sai Bhargava Reddy, M.; Zaid, M.; Das, S.; Sudhakaran, S.; Aich, S.; Pol, V. G. Hierarchical MXene-derived NTP/C nanohybrids for cryogenic sodium-ion batteries. *Adv. Funct. Mater.* **2026**, *36*, e76436. DOI
24. Li, Y.; Wang, L.; Sun, Z.; et al. Capacitance-enhanced battery: integrating high-density battery capacity with supercapacitive swiftness in an ultra-large MXene architecture. *Adv. Mater.* **2025**, *37*, e08336. DOI
25. Li, Y.; Yuan, Z.; Li, D.; et al. Multi-interface combination of bimetallic selenide and $V_4C_3T_x$ MXene for high-rate and ultrastable sodium storage devices. *ACS. Nano.* **2024**, *18*, 4733-45. DOI
26. Kang, F.; Yan, L.; Cao, Y.; et al. Poly(*p*-benzoquinono)diimidazole-linked covalent organic framework as an efficient anode endues sodium-ion batteries with high performance and wide temperature adaptability. *J. Am. Chem. Soc.* **2025**, *147*, 26069-78. DOI
27. Shen, Z.; Bo, Z.; Shi, R.; et al. Functional p-π conjugated organic layer empowers stable sodium metal batteries. *Adv. Funct. Mater.* **2025**, *35*, 2420573. DOI
28. Moussaei, M.; Babazadeh-Mamaqani, M.; Roghani-Mamaqani, H.; Haddadi-Asl, V.; Riazi, H. Polymer grafting on MXene as a versatile nanoplatform: Synthesis and applications. *Coord. Chem. Rev.* **2025**, *544*, 216989. DOI
29. Zhang, T.; Zhang, F.; Zhang, L.; et al. High energy density Li-ion capacitor assembled with all graphene-based electrodes. *Carbon* **2015**, *92*, 106-18. DOI
30. Li, Z.; Wang, Y.; Zhao, F.; et al. Moss-like two-dimensional MBene-Ni/Co bimetallic metal-organic framework composite as efficient cathode for alkaline zinc batteries. *J. Power. Sources.* **2025**, *633*, 236437. DOI
31. Li, C.; Tang, Y.; Wang, X.; Cheng, Y.; Wang, M. S. Sodiophilic hosts with pseudocapacitive kinetics for robust anode-free sodium metal batteries. *Angew. Chem. Int. Ed.* **2026**, *65*, e9106635. DOI
32. Stuart, B. H. Organic molecules. In: Infrared spectroscopy: fundamentals and applications. Wiley; 2005. pp. 71-93. DOI
33. Titantah, J. T.; Lamoen, D. First-principles characterization of amorphous carbon nitride systems: structural and electronic properties. *Phys. Status. Solidi.* **2006**, *203*, 3191-7. DOI
34. Ashiq, A.; Walpita, J.; Vithanage, M. Functionalizing non-smectic clay via methoxy-modification for enhanced removal and recovery of oxytetracycline from aqueous media. *Chemosphere* **2021**, *276*, 130079. DOI PubMed
35. Pazdera, J.; Issayeva, D.; Titus, J.; Gläser, R.; Deutschmann, O.; Jentys, A. Impact of the local environment of amines on the activity for CO_2 hydrogenation over bifunctional basic - metallic catalysts. *ChemCatChem* **2022**, *14*, e202200620. DOI
36. Beshkov, G.; Dimitrov, D.; Georgiev, S.; et al. XPS spectra of thin CN_x films prepared by chemical vapor deposition. *Diamond. Relat. Mater.* **1999**, *8*, 591-4. DOI
37. Okpalugo, T.; Papakonstantinou, P.; Murphy, H.; Mclaughlin, J.; Brown, N. High resolution XPS characterization of chemical functionalised MWCNTs and SWCNTs. *Carbon* **2005**, *43*, 153-61. DOI
38. Ma, Y.; Liu, K.; Wang, K.; et al. Overcoming redox barriers in black phosphorus negative electrodes through lattice P-N engineering for fast-charging Li-ion batteries. *Nat. Commun.* **2026**, *17*, 5479. DOI PubMed PMC
39. Lee, M.; Park, J. H.; Park, Y. J.; et al. Borate-like terminations strengthen Mxene-silicon coupling for ultrafast and durable lithium storage. *Adv. Funct. Mater.* **2026**, *36*, e75140. DOI
40. Tian, Y.; Hou, P.; Zhang, H.; et al. Theoretical insights on potential-dependent oxidation behaviors and antioxidant strategies of MXenes. *Nat. Commun.* **2024**, *15*, 10099. DOI PubMed PMC